remote sensing

MDPI

Article

On the Use of Neumann Decomposition for Crop Classification Using Multi-Temporal RADARSAT-2 Polarimetric SAR Data

Qinghua Xie [1,2], Jinfei Wang [2,*], Chunhua Liao [2], Jiali Shang [3], Juan M. Lopez-Sanchez [4], Haiqiang Fu [5] and Xiuguo Liu [1]

1 School of Geography and Information Engineering, China University of Geosciences (Wuhan), Wuhan 430074, China; xieqh@cug.edu.cn (Q.X.); liuxg318@hotmail.com (X.L.)
2 Department of Geography, The University of Western Ontario, London, ON N6A 5C2, Canada; xnliaochunhua@gmail.com
3 Research Branch, Agriculture and Agri-Food Canada, Ottawa, ON K1A 0C6, Canada; jiali.shang@agr.gc.ca
4 Institute for Computer Research (IUII), University of Alicante, E-03080 Alicante, Spain; juanma.lopez@ua.es
5 School of Geosciences and Info-Physics, Central South University, Changsha 410083, China; haiqiangfu@csu.edu.cn
* Correspondence: jfwang@uwo.ca

Received: 8 February 2019; Accepted: 27 March 2019; Published: 31 March 2019

Abstract: In previous studies, parameters derived from polarimetric target decompositions have proven as very effective features for crop classification with single/multi-temporal polarimetric synthetic aperture radar (PolSAR) data. In particular, a classical eigenvalue-eigenvector-based decomposition approach named after Cloude–Pottier decomposition (or "$H/A/\alpha$") has been frequently used to construct classification approaches. A model-based decomposition approach proposed by Neumann some years ago provides two parameters with very similar physical meanings to polarimetric scattering entropy H and the alpha angle α in Cloude–Pottier decomposition. However, the main aim of the Neumann decomposition is to describe the morphological characteristics of vegetation. Therefore, it is worth investigating the performance of Neumann decomposition on crop classification, since vegetation is the principal type of targets in agricultural scenes. In this paper, a multi-temporal supervised classification method based on Neumann decomposition and Random Forest Classifier (named "ND-RF") is proposed. The three parameters from Neumann decomposition, computed along the time series of data, are used as classification features. Finally, the Random Forest Classifier is applied for supervised classification. For comparison, an analogue classification scheme is constructed by replacing the Neumann decomposition with the Cloude–Pottier decomposition, hence named CP-RF. For validation, a time series of 11 polarimetric RADARSAT-2 SAR images acquired over an agricultural site in London, Ontario, Canada in 2015 is employed. Totally, 10 multi-temporal combinations of datasets were tested by adding images one by one sequentially along the SAR observation time. The results show that the ND-RF method generally produces better classification performance than the CP-RF method, with the largest improvement of over 12% in overall accuracy. Further tests show that the two parameters similar to entropy and alpha angle produce classification results close to those of CP-RF, whereas the third parameter in the Neumann decomposition is more effective in improving the classification accuracy with respect to the Cloude–Pottier decomposition.

Keywords: polarimetric SAR (PolSAR); crop classification; multi-temporal; target decomposition; random forest; Cloude–Pottier decomposition; Neumann decomposition; RADARSAT-2

1. Introduction

Crops play an essential role in global economic activity, diets, biofuel and climate change [1]. Mapping the distribution and changes of cropland area can provide useful information to support the sustainable management and development of agriculture [2]. To obtain this vital information, a comprehensive, systematic and accurate global or regional monitoring technology is required [2,3]. Remote sensing has shown strong ability to observe the land in high spatial and spectral resolution, wide-range cover with a short revisit time. It has incomparable advantages with respect to the traditional field measurements and is developing rapidly to support this growing demand. In particular, synthetic aperture radar (SAR), an active microwave remote sensing technology, has the capability of operation in all-time and all-weather. It is crucial for global agriculture monitoring, especially, in case the optical sensors are limited to work, such as with persistent cloud cover, haze and none solar illumination [3]. In addition, the SAR images can provide unique structural characteristics of vegetation with respect to the optical image. For crops, radar backscatter is influenced by many factors, such as the shape and structural attributes of crops, the dielectric properties of the crop canopy and the underlying background soil, the planting density and row direction, etc. [2]. With respect to single or dual-polarization SAR, Polarimetric SAR (PolSAR) can provide richer information and sensitivity to the types of scattering mechanisms present in the scene [4,5]. Since radar response to crops is polarization dependent, the exploitation of differences in the polarization signatures for crop classification can achieve improvements of accuracy with respect to single polarization SAR data [4–6]. A number of PolSAR satellite sensors have been launched in past years, such as RADARSAT-1/2 in Canada, ALOS-1/2 in Japan, TerraSAR-X and Tandem-X in Germany, GF-3 in China, RISAT-1/2 in India, SAOCOM-1/2 in Argentina, etc. In addition, some airborne PolSAR platforms have been developed as well. Based on these abundant PolSAR datasets, plenty of studies employing polarimetric features with single/multi-temporal data for crop classification have been reported in the literature [6–21].

A widely used approach for obtaining polarimetric features is polarimetric target decomposition. It can be classified into two main categories: coherent decompositions based on the single-look Sinclair scattering matrix and incoherent decompositions based on a multi-look scattering matrix, i.e., coherency/covariance matrix [4,22]. The first category of approaches is used for describing a "pure single target" or stationary target in the scene, ignoring the high speckle noise effect associated with single-look imagery. The representative coherent decomposition approaches include Pauli, Krogager and Cameron decompositions [4]. In contrast, the second category of approaches is used for describing distributed targets. Due to the capability of considering the combination of inherent coherent speckle noise and random vector scattering effects from surface and volume, the incoherent decomposition approaches are more suitable for interpreting most targets in natural media. The model-based and eigenvalue-eigenvector-based decomposition are two subcategories within the incoherent decomposition approaches [4,22]. Model-based decompositions represent the measured coherency/covariance matrix as a linear combination of some canonical scattering mechanisms described with scattering models. By applying different scattering models, different decomposition solutions are obtained [22]. The Freeman–Durden three-component decomposition is the pioneering model-based decomposition method, which defines three scattering models to represent surface scattering, double-bounce scattering and volume scattering in the scene [23]. Afterwards, plenty of improvements to enhance decomposition performance have been proposed [24–33]. The obtained scattering powers from different scattering components can be used as features for crop classification. Instead, the eigenvalue-eigenvector-based decomposition is based on the eigenvalues and eigenvectors of the measured coherency matrix, which is roll-invariant and has a clearer mathematical background [4,22]. The Cloude–Pottier decomposition is the most representative method in this category [4,34]. Based on this decomposition, three polarimetric parameters with clear physical interpretations, including the polarimetric scattering entropy H, the alpha angle α and the polarimetric anisotropy A are derived. The polarimetric scattering entropy H ($0 \leq H \leq 1$) is an indicator to measure the degree of scattering randomness in the scattering medium. A larger value of

H means higher scattering randomness. The alpha angle α ($0 \leq \alpha \leq 90°$) is an indicator of the type of scattering mechanism in the scene. Based on both two parameters, an H/α plane is proposed to represent all random scattering mechanisms and used for designing an unsupervised classification scheme [4,34–36]. The polarimetric anisotropy A ($0 \leq A \leq 1$) measures the relative importance between the secondary scattering mechanisms. It should be noted that A becomes a very useful parameter to help to distinguish different scattering types only for medium values of H [4,34]. In this case, the secondary scattering mechanisms play an important role in the scattering process. Consequently, the Cloude–Pottier decomposition is frequently called "H/α" or "H/A/α" decomposition in the literature. Based on the physical properties of these parameters, there are also studies which exploit the Cloude–Pottier decomposition for crop classification [17–21].

Some years ago, a model-based decomposition method proposed by Neumann can produce two output parameters which have similar physical meaning to the first two parameters, H and α, produced by the Cloude–Pottier decomposition [37–40]. The key contribution of the Neumann decomposition is proposing a generalized volume scattering model for describing the morphological characteristics of vegetation, which is defined by two parameters: the particle scattering anisotropy δ and the degree of orientation randomness τ. In general, the magnitude of the particle scattering anisotropy $|\delta|$ indicates the effective shape of an average particle. In addition, it could also be used to describe the type of scattering mechanism in the scene, since there exists a direct mathematic transformation relationship to the alpha angle α in Cloude–Pottier decomposition [37–40]. On the other hand, the phase of the particle scattering anisotropy ϕ_δ is more related to the orientation direction of the particles [37,39]. The degree of orientation randomness τ ($0 \leq \tau \leq 1$) is also an indicator of the degree of scattering randomness, which is related to the polarimetric scattering entropy H in Cloude–Pottier decomposition. Since the Neumann decomposition starts from the emphasis on describing vegetation scattering and has a physical meaning close to Cloude–Pottier decomposition, it is worthy of investigating the performance of Neumann decomposition on the application of crop classification, in which vegetation is the principal type of target in the scene. In addition, multi-temporal datasets are usually exploited for improving crop classification accuracies because they enable the incorporation of information about the temporal changes in the structure and dielectric features of the crops during their whole growing season [14,16–18,20]. Moreover, the change information of different crop types shows significant difference due to inherent differences in phenological characteristics. Therefore, multi-temporal data usually show stronger ability to discriminate different crop types than single-date data.

Based on these motivations, a multi-temporal supervised classification method based on Neumann decomposition and Random Forest Classifier (named as "ND-RF") for crop classification is proposed in this paper. In this approach, the Neumann decomposition is used for providing three polarimetric parameters ($|\delta|$, τ, ϕ_δ) as classification features. The Random Forest Classifier is applied for supervised classification. For comparison, the CP-RF classification scheme is constructed by replacing the three parameters of the Neumann decomposition by the three parameters from Cloude–Pottier decomposition (H, α, A).

The structure of this paper is organized as follows. In Section 2, the descriptions of the study site and the multi-temporal RADARSAT-2 dataset are presented. Then, the details of the proposed ND-RF classification method are introduced in Section 3. The relationship between parameters from Neumann decomposition and Cloude–Pottier decomposition are also provided in this section. In Section 4, the classification performances obtained by ND-RF and CP-RF methods are analyzed. In Section 5, the classification in case of only using two parameters (τ, $|\delta|$ or H, α), with close physical meaning, as classification features is analyzed and discussed. Finally, conclusions are drawn in Section 6.

2. Study Site and RADARSAT-2 Dataset

2.1. Study Site Description

The study site is located in London, Ontario, Canada (Lat/Lon, N42.8°/W81.5°) and the Pauli RGB image from 12 April 2015 is shown in Figure 1. It is an agricultural area, covered by a variety of crops, few buildings and forests. The dominant crops correspond to four types: winter wheat, corn, soybean and forage, including alfalfa and grass, which totally take up over 90% of the planting area. In addition, there are few fields of tobacco and watermelon in the site. The study site is very productive for agriculture because of abundant precipitation, fertile soil and relatively mild weather. The agricultural activity in this site is generally regular year by year. In general, the seeding and harvest dates for corn and soybean are around May and October, respectively. In particular, winter wheat is seeded in October the previous year and harvested in July the following year. In addition, winter wheat usually is seeded in harvested soybean fields for crop rotation, which results in some changes for crop types of some fields after October.

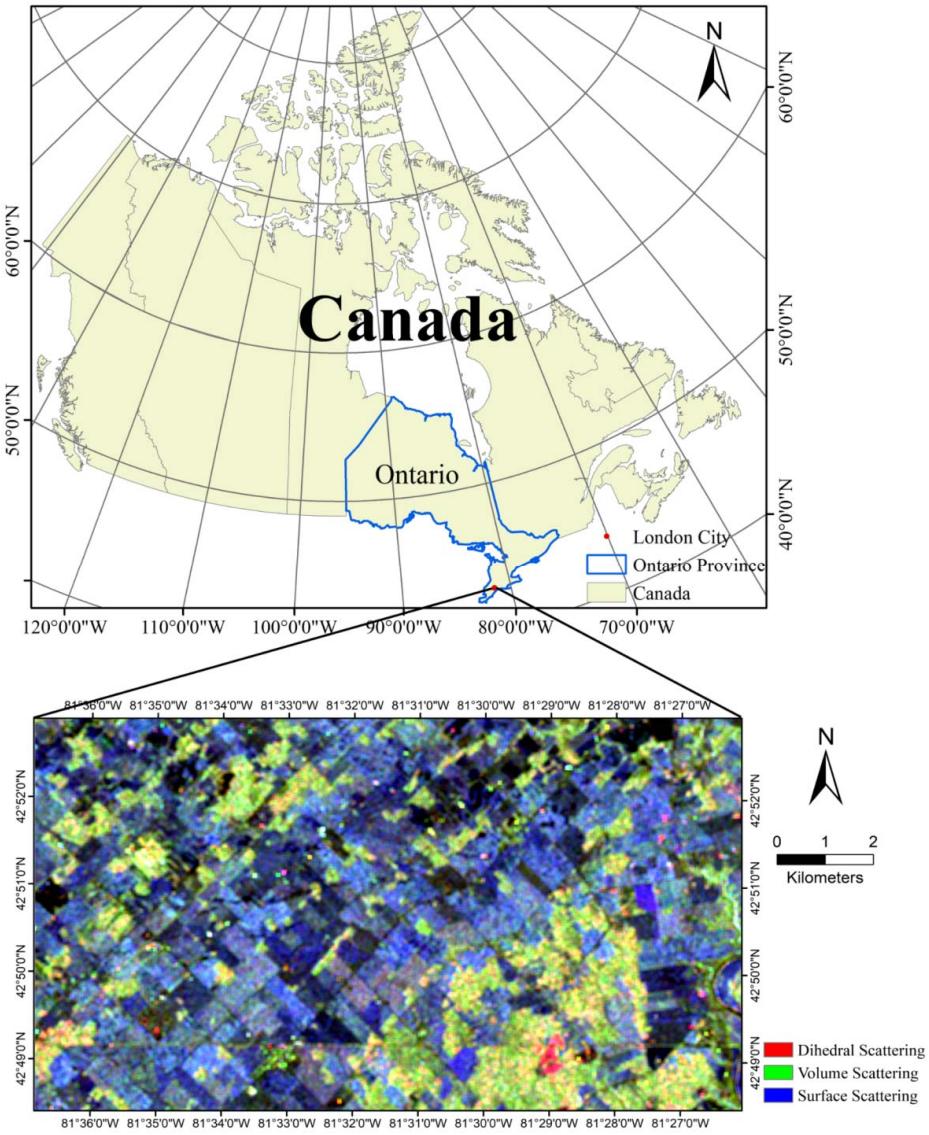

Figure 1. Location and Pauli RGB image acquired on 12 April 2015 of the study site.

2.2. RADARSAT-2 Dataset Description

Since crop rotation introduces some changes in crop types in October, a total of 11 fine-quad wide beam mode (FQW) RADARSAT-2 Polarimetric SAR images were acquired from 12 April to 27 September in 2015 for crop classification purpose. This time interval basically covers the entire growing cycle of main crops in the study site. Regarding the beam mode, there are some differences among the acquired images. The details are shown in Table 1.

Table 1. The acquired RADARSAT-2 polarimetric SAR data description.

Date	Mode	Incidence (Degree)	Resolution (Az (m) × Rg (m))	Orbit	Look Direction
20150412	FQ10W	28.391~31.575	5.479 × 4.733	Ascending	Right
20150506	FQ10W	28.389~31.573	5.479 × 4.733	Ascending	Right
20150520	FQ1W	17.494~21.155	4.828 × 4.733	Ascending	Right
20150623	FQ10W	28.389~31.573	5.479 × 4.733	Ascending	Right
20150703	FQ20W	38.643~41.274	5.066 × 4.733	Ascending	Right
20150717	FQ10W	28.388~31.572	5.479 × 4.733	Ascending	Right
20150810	FQ10W	28.391~31.574	5.479 × 4.733	Ascending	Right
20150903	FQ10W	28.385~31.569	5.479 × 4.733	Ascending	Right
20150913	FQ20W	38.642~41.274	5.066 × 4.733	Ascending	Right
20150917	FQ1W	17.487~21.149	4.828 × 4.733	Ascending	Right
20150927	FQ10W	28.387~31.572	5.479 × 4.733	Ascending	Right

2.3. Ground-Truth Description

From April to September 2015, field surveys were carried out every month. Information including crop-type, ground photos, weather condition, soil moisture content, and crop phenological stage was recorded. In addition, two intensive landcover surveys were conducted in September. As shown in Figure 2, in the overlapping area of all RADARSAT-2 images, the landcover types of 85 fields were identified, with 20 corn fields, 16 soybean fields, 12 forage fields, 19 winter wheat fields, 10 forest fields, 2 bare soil fields, 2 watermelon fields, 2 tobacco fields and 2 built-up fields. Training and testing samples were randomly selected without overlap (i.e., from different fields) for classification and accuracy assessment. Detailed information is shown in Table 2.

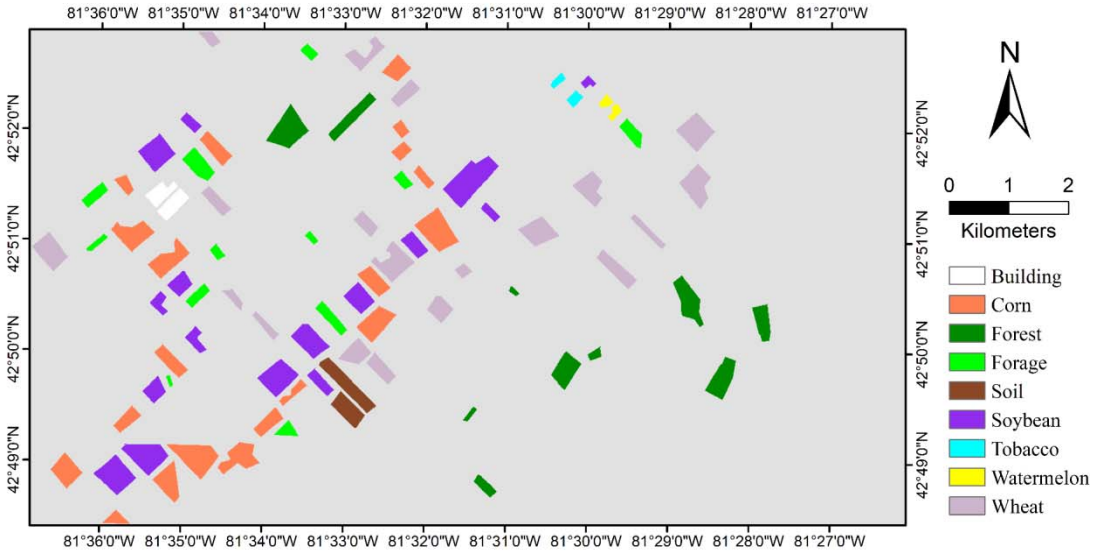

Figure 2. Map of identified land-cover types.

Table 2. The collected field data and the number of pixels for classification training and testing.

Land Cover	Training Samples		Testing Samples	
	Number of Pixels	Number of Fields	Number of Pixels	Number of Fields
Corn	6258	4	20,246	16
Soybean	6505	4	15,995	12
Forage	3700	5	3615	7
Winter wheat	6018	3	17,723	16
Watermelon	310	1	309	1
Tobacco	416	1	301	1
Forest	5148	4	7292	6
Built-up	1267	1	1117	1
Soil	2331	1	1592	1

3. Methodology

The proposed Neumann decomposition based Random Forest (RF) Multi-temporal Classification Method (ND-RF) consists of data preprocessing, Neumann decomposition and RF classification. The workflow of the proposed ND-RF method is shown in Figure 3.

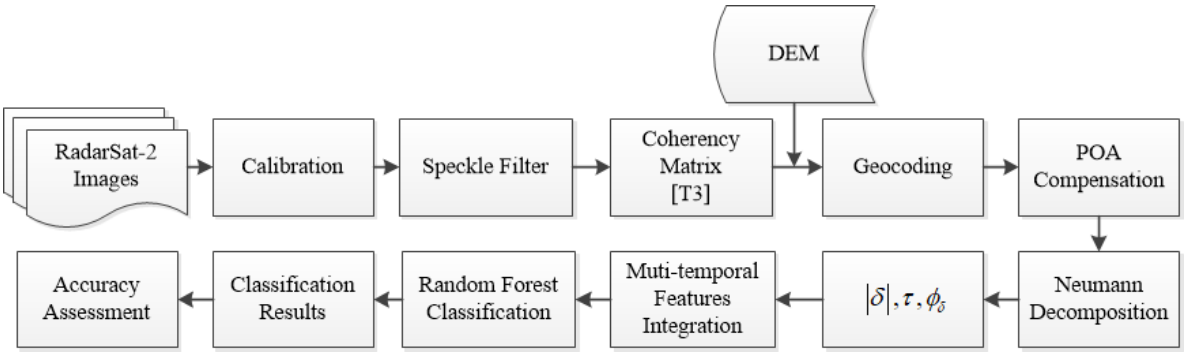

Figure 3. Workflow of the proposed Neumann decomposition and Random Forest Classifier (ND-RF) classification method used in this study.

3.1. Data Preprocessing

For every RADARSAT-2 image, the pixel values for four polarization channels (HH, HV, VH and VV) were first calibrated to sigma naught. Then, a 9×9 boxcar filter was applied to reduce the inherent speckle noise. The corresponding polarimetric coherency matrix for every pixel of every image was then generated. A province Digital Elevation Model (PDEM) of Ontario province, Canada with a resolution of 30 m covering the study site was used for geocoding all coherency matrices in UTM geographic reference. Finally, for multi-temporal classification, the area of interest covering the field survey area was selected from the overlapping region among all RADARSAT-2 images. Subsequent decomposition processing was conducted over the area of interest to extract polarimetric features for classification.

3.2. Neumann Decomposition

In a fully polarimetric SAR system, the acquired scattering matrix in H-V polarization basis can be expressed as [4,5]

$$S = \begin{bmatrix} S_{HH} & S_{HV} \\ S_{VH} & S_{VV} \end{bmatrix} \quad (1)$$

where S_{ij} $(i, j = H \text{ or } V)$ represents the scattering coefficient from transmitting with i polarization and receiving with j polarization. After assuming the reciprocal scattering (i.e., $S_{HV} = S_{VH}$), the corresponding Pauli-basis vector can be expressed as [4,5]

$$k_P = \frac{1}{\sqrt{2}}\begin{bmatrix} S_{HH}+S_{VV} & S_{HH}-S_{VV} & 2S_{HV} \end{bmatrix} \tag{2}$$

Then, the corresponding coherency matrix is given as [4,5]

$$\begin{aligned} T &= \langle k_P k_P^{*T} \rangle \\ &= \frac{1}{2}\begin{bmatrix} \left\langle |S_{HH}+S_{VV}|^2 \right\rangle & \langle (S_{HH}+S_{VV})(S_{HH}-S_{VV})^* \rangle & 2\langle (S_{HH}+S_{VV})S_{HV}^* \rangle \\ \langle (S_{HH}-S_{VV})(S_{HH}+S_{VV})^* \rangle & \left\langle |S_{HH}-S_{VV}|^2 \right\rangle & 2\langle (S_{HH}-S_{VV})S_{HV}^* \rangle \\ 2\langle S_{HV}(S_{HH}+S_{VV})^* \rangle & 2\langle S_{HV}(S_{HH}-S_{VV})^* \rangle & 4\left\langle |S_{HV}|^2 \right\rangle \end{bmatrix} \end{aligned} \tag{3}$$

Some years ago, Neumann proposed a model-based incoherent PolSAR decomposition method whose key contribution is the introduction of a generalized volume scattering model, which is defined by two parameters: the particle shape and the orientation randomness [37–39]. Similar to the basic principle of the volume scattering modelling in Freeman–Durden or Yamaguchi-based methods, the Neumann volume scattering model is based on assuming the volume as a cloud of randomly oriented particles, and the orientation angle follows a certain statistic distribution. The normalized coherency matrix for one scattering particle in the volume is defined as [37–39]

$$T_\delta = \begin{bmatrix} 1 & \delta & 0 \\ \delta^* & |\delta|^2 & 0 \\ 0 & 0 & 0 \end{bmatrix} \tag{4}$$

where δ is the particle scattering anisotropy, of which the magnitude indicates the effective shape of an average particle. In general, when $|\delta|$ is close to zero, the effective shape tends toward an isotropic sphere/disk. As $|\delta|$ approaches one, the effective shape is close to a dipole (i.e., thin cylinder). The sign of real part of δ determines the tendency of the particle axis of symmetry. It tends to be horizontal for $\mathrm{Re}(\delta) > 0$ and vertical for $\mathrm{Re}(\delta) < 0$. The phase of δ, i.e., ϕ_δ, is more related to the orientation direction of the particles. From the mathematic point of view, it can be seen that ϕ_δ is related to the sign of real part of δ. For $\phi_\delta \in [0, \pi]$, the particles tends to be horizontal ($\mathrm{Re}(\delta) > 0$) and vertical ($\mathrm{Re}(\delta) < 0$) for $\phi_\delta \in [-\pi, 0]$. In Freeman–Durden or Yamaguchi-based methods [23–27], the scattering particle is one specific case, which assumes the scatterer is horizontal or vertical dipole, i.e., $\delta = \pm 1$. Since the tendency somehow represents the morphological structure information, obviously it depends on the vegetation type. Theoretically, $\mathrm{Re}(\delta)$ or ϕ_δ can be used to help distinguishing the land cover types. However, from the perspective of independence of random variables, the magnitude and phase of δ (i.e., $|\delta|$ and ϕ_δ) are selected as classification features in this study.

Assuming the particle is rotated by an angle ψ around the radar line of sight (Los), the coherency matrix describing a cloud of volume particles can be obtained by the integration of coherence matrix of a single particle over the orientation angles.

$$T_v = \int_{-\pi/2}^{\pi/2} R_3(\psi) T_\delta R_3(\psi)^T P(\psi) \tag{5}$$

where $R_3(\psi)$ is the rotation matrix and $P(\psi)$ is the probability distribution function of orientations of the volume scatterers. Under the central limit theorem condition, Neumann suggests the orientation angle of volume scatterers follows a von Mises distribution (also known as the circular normal distribution), which can be expressed as [37–39]

$$p(\psi|\widetilde{\psi}, \kappa) = \frac{e^{\kappa \cos(2(\psi - \widetilde{\psi}))}}{\pi I_0(\kappa)}, \ \kappa \in [0, \infty] \tag{6}$$

where κ represents the degree of concentration, $\widetilde{\psi}$ is the mean orientation angle, and $I_0(\kappa)$ denotes the modified Bessel function of order zero. For a simple geometrical interpretation, the normalized degree of orientation randomness τ is defined as [37–39]

$$\tau = I_0(\kappa)e^{-\kappa}, \ \ \tau \in [0,1] \tag{7}$$

With the variation of τ, the volume can change from a preferred orientation direction ($\tau = 0$) to completely random ($\tau = 1$). Under the linear approximation for the orientation distribution, one can obtain two linear models for the coherency matrix form [33,37–39]

$$T_v(\delta,\tau) = \begin{cases} \frac{1}{1+|\delta|^2}\begin{bmatrix} 1 & (1-\tau)\delta & 0 \\ (1-\tau)\delta^* & (1-\tau)|\delta|^2 & 0 \\ 0 & 0 & \tau|\delta|^2 \end{bmatrix} & \tau \le \frac{1}{2} \\ \frac{1}{1+|\delta|^2}\begin{bmatrix} 1 & (1-\tau)\delta & 0 \\ (1-\tau)\delta^* & \frac{1}{2}|\delta|^2 & 0 \\ 0 & 0 & \frac{1}{2}|\delta|^2 \end{bmatrix} & \tau > \frac{1}{2} \end{cases} \tag{8}$$

where the sum of diagonal elements is one. From Equation (8), it can be seen that Neumann generalized volume scattering model depends on two morphological vegetation parameters: δ and τ. As it was analyzed in [37,38], the Neumann general vegetation model agrees with some typical models. When τ is equal to one, i.e., completely random case, it is the same as the volume scattering model in Freeman two-component decomposition. Two Yamaguchi volume scattering models are also approximately considered as two special cases of it [37,38].

It should be noted that Neumann generalized volume scattering model could be incorporated in any PolSAR/PolInSAR model-based decomposition framework [33]. However, the Neumann decomposition is generally employed by matching completely the Neumann volume scattering model to the observed coherency matrix in order to directly invert two model parameters. In this case, the parameters from Neumann decomposition are defined as [37–39]

$$|\delta| = \sqrt{\frac{T_{22}+T_{33}}{T_{11}}} = \left| \sqrt{\frac{\left\langle |S_{\mathrm{HH}} - S_{VV}|^2 \right\rangle + 4\left\langle |S_{HV}|^2 \right\rangle}{\left\langle |S_{HH} + S_{VV}|^2 \right\rangle}} \right| \tag{9}$$

$$\tau = 1 - \frac{|T_{12}|}{|T_{11}||\delta|} = 1 - \frac{1}{|\delta|}\frac{\left|\left\langle (S_{\mathrm{HH}} + S_{VV})(S_{\mathrm{HH}} - S_{VV})^* \right\rangle\right|}{\left\langle |S_{HH} + S_{VV}|^2 \right\rangle} \tag{10}$$

$$\phi_\delta = Arg(T_{12}) \tag{11}$$

Then, the particle scattering anisotropy magnitude and phase (i.e., $|\delta|$ and ϕ_δ), and the orientation randomness τ are adopted in this work as three polarimetric features for crop classification. In addition, in order to reduce the effects of overestimation of cross-scattering due to some uncertain reasons, such as topography slopes, it is usual to carry out the polarimetric orientation angle (POA) compensation (also called deorientation processing) proposed by Lee et al. [41] before the Neumann decomposition.

It can be proven that these parameters are related to other existing scattering models and scattering mechanism types. In [37–39], Neumann found that two of polarimetric feature parameters derived from Neumann decomposition have close relationships with the classical and commonly used Cloude–Pottier decomposition. The basic idea of Cloude–Pottier (CP) decomposition is to express the observed coherency matrix as a sum of three independent targets according to eigenvector and eigenvalue analysis. Then, this decomposition can be described as [4,5,34]

$$T = \sum_{i=1}^{3} \lambda_i u_i u_i^{*T} \tag{12}$$

where λ_1, λ_2 and λ_3 are three eigenvalues of coherency matrix and $\lambda_1 \geq \lambda_2 \geq \lambda_3$. The corresponding three eigenvectors are u_1, u_2 and u_3. Then, the polarimetric scattering entropy H, averaged alpha angle α and polarimetric anisotropy A are defined as [4,5,34]

$$H = \sum_{i=1}^{N} -P_i \log_N P_i, \; where \; P_i = \frac{\lambda_i}{\sum_{j=1}^{N} \lambda_i} \tag{13}$$

$$\alpha = \sum_{i=1}^{3} P_i \alpha_i \tag{14}$$

$$A = \frac{\lambda_2 - \lambda_3}{\lambda_2 + \lambda_3} \tag{15}$$

where α_i can be determined by the eigenvectors because $\cos(\alpha_i)$ is same as the magnitude of the first component of the eigenvector u_i. The polarimetric scattering entropy H indicates the scattering randomness degree. It ranges from 0 to 1, which represents from specifically identifiable scattering or deterministic scattering to complete random scattering. The value of angle α represents the scattering mechanism types in the scattering medium, which ranges from 0 (surface scattering) to 90° (double-bounce scattering). In particular, as it reaches the medium value of 45°, it represents dipole scattering or linearly-polarized scattering by a cloud of anisotropic particles [4,34]. The polarimetric anisotropy A ranges from 0 to 1, which measures the relative importance between the secondary scattering mechanisms. It should be noted that A becomes a very useful parameter to help to distinguish different scattering types only for medium values of H [4,34]. In this case, the secondary scattering mechanisms play an important role in the scattering process.

Afterward, Neumann found the particle scattering anisotropy magnitude $|\delta|$ to be directly related to the α angle in CP decomposition, i.e., [37–40]

$$|\delta| = \tan(\alpha) \tag{16}$$

The parameter $|\delta|$ either represents the shape of the particle, if volumetric particle scattering is assumed, or the scattering mechanism type, if a mixed scattering mechanism is assumed. In theory, the range of $|\delta|$ is assumed to be restricted within [0,1] under the Born approximation for a cloud of simple spheroidal particles. As it is an indicator for multiple scattering effects in the canopy, which are neglected by the Born approximation, the value of $|\delta|$ could be larger than 1 [39]. The general relationship between $|\delta|$ and α is shown in Table 3.

Table 3. The general relationship between $|\delta|$ and α.

$\|\delta\|$	α	**Scattering Mechanism**
0	0	Surface scattering
1	45°	Dipole scattering
∞	90°	Double-bounce scattering

From the definition of orientation randomness τ in Neumann decomposition and polarimetric scattering entropy H in Cloude–Pottier decomposition, it is easy to understand that both parameters describe the scattering randomness in the scattering medium. Figure 4 shows the dependence of polarimetric scattering entropy H on the orientation randomness τ with different value of the particle scattering anisotropy magnitude. It can be seen that generally the values of polarimetric scattering entropy H will monotonically rise with an increase of orientation randomness τ. In particular, the values of orientation randomness become meaningless for $|\delta| = 0$ because the effective particle shape is considered as the isotropic scatterer in that case. Moreover, as the effective particle shape varies from isotropic scatterer ($|\delta| = 0$) to dipole scatterer ($|\delta| = 1$), the degree of scattering randomness in the medium increases gradually.

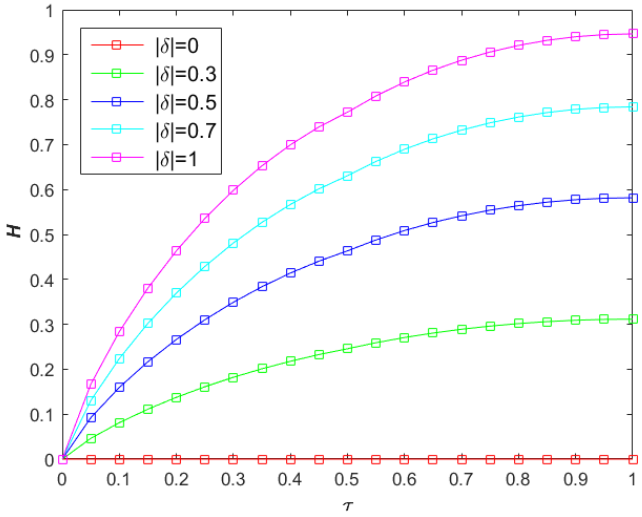

Figure 4. Dependence of polarimetric scattering entropy H on the orientation randomness τ with different values of the particle scattering anisotropy magnitude.

From the analysis mentioned above, it is clear that the two parameters (τ, $|\delta|$) derived from Neumann decomposition have significant correlation with the two parameters (H, α) derived from Cloude–Pottier decomposition. In addition, the third parameter (ϕ_δ or A) in Neumann decomposition or Cloude–Pottier decomposition can also enhance the ability in distinguishing land cover types. The parameters derived from Cloude–Pottier decomposition are frequently used in land cover classification studies. In this regard, Neumann decomposition parameters should have the potential for land cover classification.

3.3. Random Forest Classification

Before classification, the three polarimetric features from Neumann decomposition ($|\delta|$, τ, ϕ_δ) or Cloude–Pottier decomposition (H, α, A) were computed for every image. Therefore, when all images are considered, a feature vector with 33 bands for every pixel was used for classification. Although there are many classification methods for crop classification using PolSAR data, the well-known Random Forest (RF) Classifier was selected in this study due to its good performance and demonstrated advantages in crop-type mapping [15–18]. The RF classifier is an ensemble learning classification method, which creates a set of decision trees from randomly selected subsets of input training features [42,43]. The output class for the testing pixel is decided by aggregating the votes from individual decision trees. It generally provides high classification accuracy, even if the size of the training samples is small. For a large dataset, it also runs efficiently and produces highly accurate results. Moreover, it can additionally provide estimates of the variable importance in the classification [15–18,42,43]. Although increasing the number of trees usually will increase the classification accuracy, it will increase the computational burden as well. Previous studies have proven that accuracy improves much slowly as the number of trees is over 50 [17,18]. Consequently, an RF with 100 decision trees was selected in this study.

4. Experiment Results

From the theoretical analysis in Section 3, it is clear to see that polarimetric parameters from Neumann decomposition have tight relationships in physical phenomena with the ones from the classical Cloude–Pottier decomposition. Therefore, in addition to testing the proposed ND-RF classification method, we also tested the CP-RF classification method for comparison purposes. Compared with the flowchart of the ND-RF classification method, the so-called CP-RF classification is constructed by simply replacing the Neumann decomposition with Cloude–Pottier decomposition

(see Figure 3). In that case, H, α and A are adopted as input features. It should be noticed that the POA compensation step can be neglected in the CP-RF method because the Cloude–Pottier decomposition is roll-invariant.

In a study with multi-temporal data, the number of images for constructing the multi-temporal dataset will naturally affect the classification results. Moreover, it is worthy of studying the time-series performance while assessing the classification accuracies of different methods. For these reasons, 10 multi-temporal combinations of datasets were constructed by adding images one by one in sequence along the SAR observation time. For each multi-temporal combination, the ND-RF and CP-RF classification methods were applied, and the corresponding accuracy assessments were carried out. The corresponding classification performance of both two methods are shown as follows.

4.1. Overall Classification Performance

Table 4 shows the overall accuracy and Kappa coefficient of the ND-RF and CP-RF classification methods for all 10 combinations of multi-temporal RADARSAT-2 images. From this table, it is clear to see that the classification accuracy of both ND-RF and CP-RF improves with the increase of the number of images. The largest improvements are found at the beginning, and then changes become gradual. The reason can be attributed to the degree of change in the crop characteristics, which is the main resource to provide extra feature difference information in the time dimension. At the beginning, the winter wheat is short and other crops are almost like bare soil. Since the feature differences in different crops are not significant, the overall classification accuracies are low. As time increases, the physical properties and morphological characteristics of all fields change gradually. As a result, the feature difference information makes effect. In the late time, the wheat has been harvested and other crops are almost achieving the final phenological stage, i.e., the physical property and morphological characteristics are almost unchanged. In this case, the classification results improve less whatever classification method is used.

Table 4. The overall accuracy and Kappa coefficient of ND-RF and CP-RF classification methods with different combinations of multi-temporal RADARSAT-2 images.

Multi-Temporal Combination	Number of Images	ND-RF		CP-RF	
		OA (%)	Kappa	OA (%)	Kappa
20150412~20150506	2	53.48	0.42	46.00	0.33
20150412~20150520	3	61.49	0.51	59.60	0.49
20150412~20150623	4	75.38	0.68	69.85	0.61
20150412~20150703	5	82.71	0.78	70.34	0.61
20150412~20150717	6	87.55	0.84	76.81	0.70
20150412~20150810	7	90.33	0.87	81.77	0.76
20150412~20150903	8	91.61	0.89	84.29	0.80
20150412~20150913	9	93.47	0.92	89.75	0.87
20150412~20150917	10	93.54	0.92	90.66	0.88
20150412~20150927	11	94.12	0.92	91.86	0.89

With regard to the comparison of classification accuracy between the ND-RF and CP-RF methods, the ND-RF method produces better classification performance than the CP-RF method for all multi-temporal combinations in our study. The largest improvement of overall accuracy is over 12% when the number of images reaches five. The smallest improvement is only 2% and corresponds to the use of the whole set of images (i.e., the last case). These results suggest that the three polarimetric parameters from Neumann decomposition are generally more appropriate to represent the differences between crops, which entails better classification accuracies.

For a detailed comparison, the case of best classification performance, i.e., using all 11 RADARSAT-2 images, is selected for illustration. The corresponding classification maps using ND-RF method and CP-RF method in this case are shown in Figures 5 and 6, respectively. From both figures, one can

see that the overall clustering patterns are good, the crop fields are discriminated well, and there exists some scattered errors. To quantitatively assess the classification results, the corresponding confusion matrix of ND-RF method and CP-RF method are shown in Tables 5 and 6, respectively. It can be seen from both tables that the overall accuracy and kappa coefficient of the proposed ND-RF method are 94.12% and 0.92, which are better than the CP-RF method (91.86% and 0.89). In detail, all user's accuracies or producer's accuracies for forest and the three main economic crops (corn, soybean and wheat) are high. Every value is at least over 90%. Both two methods produce relatively low classification accuracy in forage fields. One reason is that forage type itself is complicated, since it includes alfalfa and different types of grass in the study area. The other reason is wheat growing in the early stage has similar morphological characteristics with grass. For corn, watermelon, tobacco and forest fields, the user's accuracies from the proposed ND-RF method are larger than the results from CP-RF method, while the corresponding producer's accuracies are little worse but still comparable. In contrast, the performances of the user's accuracy and producer's accuracy are opposite in wheat, soybean and building areas. For soil fields and forage fields, the user's accuracy and producer's accuracy from ND-RF method both achieve better performance than CP-RF method. In summary, the accuracy indicators of the proposed ND-RF method in most of landcover types and from an overall perspective are better than the CP-RF method.

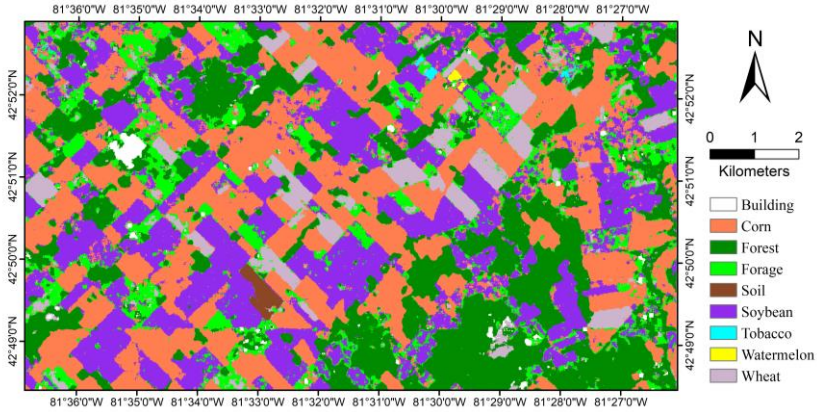

Figure 5. The classification map using ND-RF method with all 11 RADARSAT-2 images.

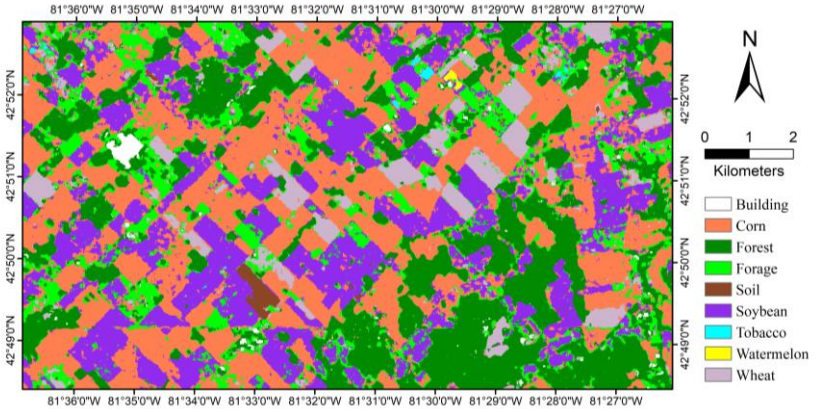

Figure 6. The classification map using CP-RF method with all 11 RADARSAT-2 images.

Table 5. The confusion matrix for the land cover mapping obtained using ND-RF method using all 11 RADARSAT-2 images (B, built-up; C, corn; F, forest; FG, forage; S, soil; SB, soybean; T, tobacco; WM, watermelon; W, wheat).

Class	Ground Truth										
	B	**C**	**F**	**FG**	**S**	**SB**	**T**	**WM**	**W**	**Tol**	**UA (%)**
B	884	0	12	3	0	0	0	0	0	899	98.33
C	0	19,324	0	432	9	93	15	23	238	20,134	95.98
F	149	2	7272	44	0	7	32	0	6	7512	96.81
FG	74	97	2	2578	40	133	55	33	823	3835	67.22
S	0	0	0	0	1423	0	5	0	0	1428	99.65
SB	4	790	6	115	46	15,757	20	91	22	16,851	93.51
T	0	0	0	0	0	0	149	0	0	149	100
WM	0	0	0	0	0	4	0	162	0	166	97.59
W	6	33	0	443	74	1	25	0	16,634	17,216	96.62
Tol.	1117	20,246	7292	3615	1592	15,995	301	309	17,723	68,190	
PA (%)	79.14	95.45	99.73	71.31	89.38	98.51	49.50	52.43	93.86		
OA (%)	94.12										
Kappa	0.92										

Table 6. The confusion matrix for the land cover mapping obtained using CP-RF method using all 11 RADARSAT-2 images (B, built-up; C, corn; F, forest; FG, forage; S, soil; SB, soybean; T, tobacco; WM, watermelon; W, wheat).

Class	Ground Truth										
	B	**C**	**F**	**FG**	**S**	**SB**	**T**	**WM**	**W**	**Tol**	**UA (%)**
B	870	0	6	0	0	0	0	0	0	876	99.32
C	2	19,438	0	1240	0	525	4	9	380	21,598	90.00
F	169	7	7259	138	0	6	28	0	17	7624	95.21
FG	72	157	21	1951	68	280	48	51	1049	3697	52.77
S	0	0	0	0	1392	8	5	0	0	1405	99.07
SB	1	559	6	50	74	15,142	8	82	14	15,936	95.02
T	0	0	0	0	0	24	156	0	0	180	86.67
WM	0	0	0	0	0	9	0	167	0	176	94.89
W	3	85	0	236	58	1	52	0	16,263	16,698	97.39
Tol.	1117	20,246	7292	3615	1592	15,995	301	309	17,723	68,190	
PA (%)	77.89	96.01	99.55	53.97	87.44	94.67	51.83	54.05	91.76		
OA (%)	91.86										
Kappa	0.89										

4.2. Classification Performance on Different Land-Cover Types

Figure 7 illustrate, as a function of the different combination of multi-temporal RADARSAT-2 images, the evolution of user's accuracies and producer's accuracies of both ND-RF and CP-RF classification methods for different land-cover types. It can be seen that the ND-RF method can produce better user's accuracies and producer's accuracies than the CP-RF method in most of cases. Moreover, the performance in terms of these accuracies increases sooner for ND-RF than for CP-RF when additional images are added. The reason could be attributed to the advantages of Neumann decomposition on its specific description of vegetation.

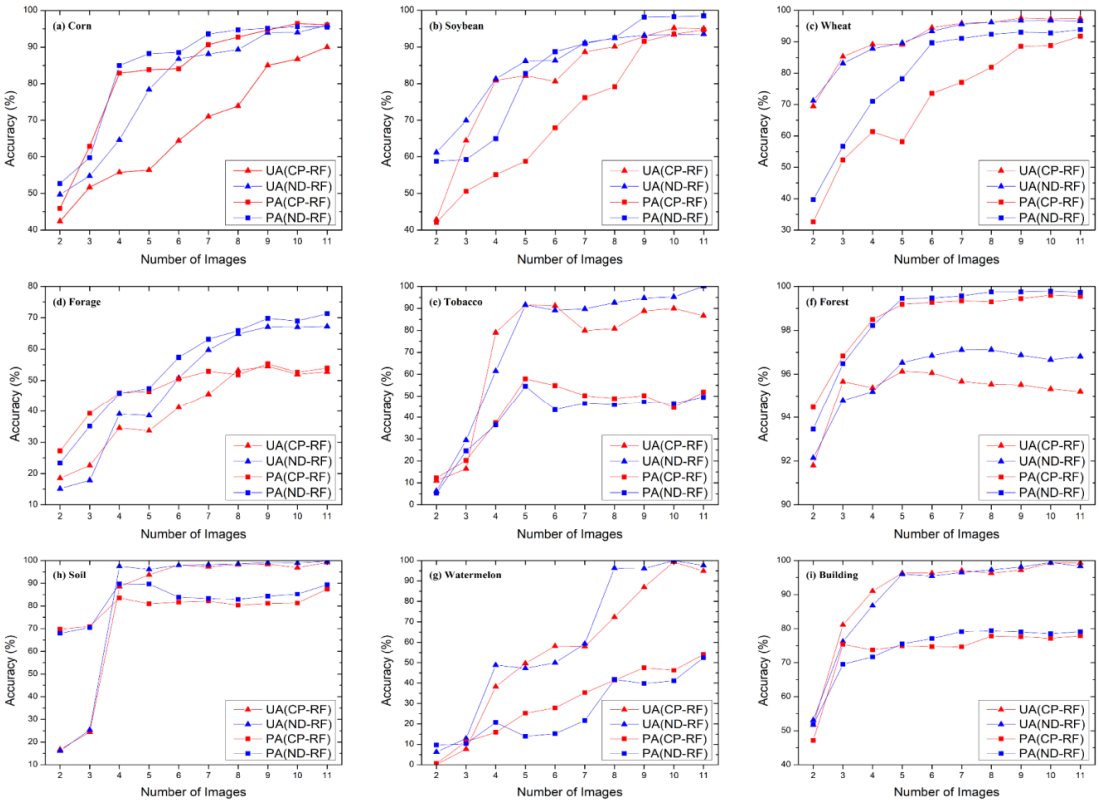

Figure 7. The user's accuracies or producer's accuracies of ND-RF and CP-RF classification methods for different land-cover types using different combinations of multi-temporal RADARSAT-2 images. (**a**) Corn, (**b**) soybean, (**c**) wheat, (**d**) forage, (**e**) tobacco, (**f**) forest, (**h**) soil, (**g**) watermelon and (**i**) building.

To understand the effect of the time of imaging on the classification accuracy, the three main economic crops (corn, soybean and wheat) are selected for further analysis. The ground truth photos of wheat, corn and soybean covers are shown in Figures 8–10, respectively. It should be noted that the dates of taking photos sometimes are not the exact dates of RADARSAT-2 observations, due to limitations from weather, human resources and other reasons. Since the maximum bias of date is only four days (occurred in June), it is acceptable to use these ground truth photos as the references to analyze the classification results. From these photos, it is clear that the available RADARSAT-2 images basically cover the whole phenological cycles of these three crops. In April and the beginning of May, the corn and soybean fields correspond to bare soil. The wheat fields are harvested in late July and is bare soil with residuals in August. Compared with the classification accuracies of these three crops in Figure 7, it can be found that the classification accuracies improve gradually with the growth of crops. For three crops, the improvements are large especially in the early dates, and become smaller in the late dates. However, the inflection points of improvement curves vary in different crops. In detail, the curve of accuracies increases significantly when the number of images is 4 (June 23) for corn and soybean, and when it is 3 (May 20) for wheat. At that time, all three crops exhibit large leaves and distribute densely. Furthermore, the curves become flat when the number of images is 9 (September 13) for corn and soybean, and when it is 7 (August 10) for wheat. At that time, corn and soybean are almost matured, and wheat is just harvested. This pattern indicates the time of imaging played an essential role in the classification, and a dataset covering the whole phenological cycle can produce high accuracy.

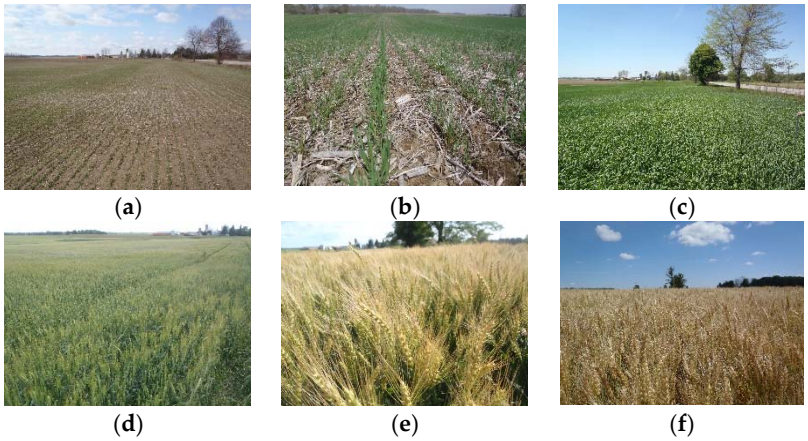

Figure 8. The ground truth photos of wheat. (**a**) April 11, (**b**) May 6, (**c**) May 23, (**d**) June 19, (**e**) July 2 and (**f**) July 16.

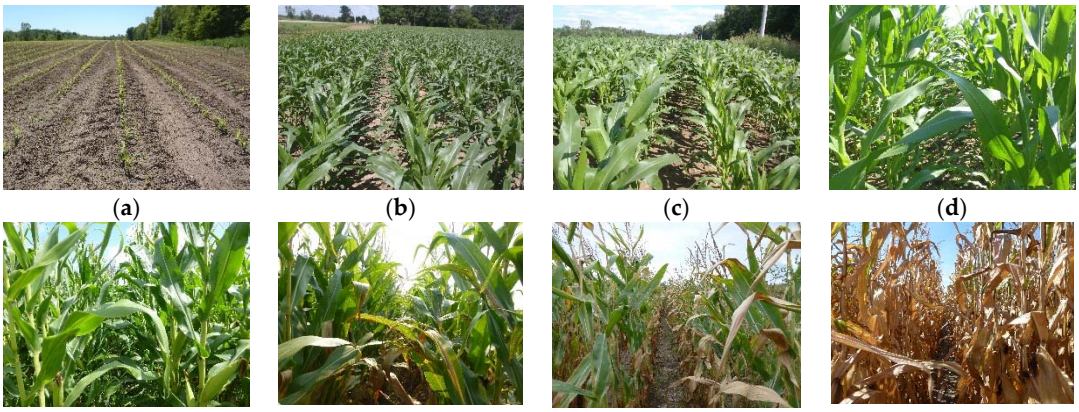

Figure 9. The ground truth photos of corn. (**a**) May 23, (**b**) June 19, (**c**) July 2, (**d**) July 16, (**e**) August 11, (**f**) September 3, (**g**) September 13 and (**h**) September 25.

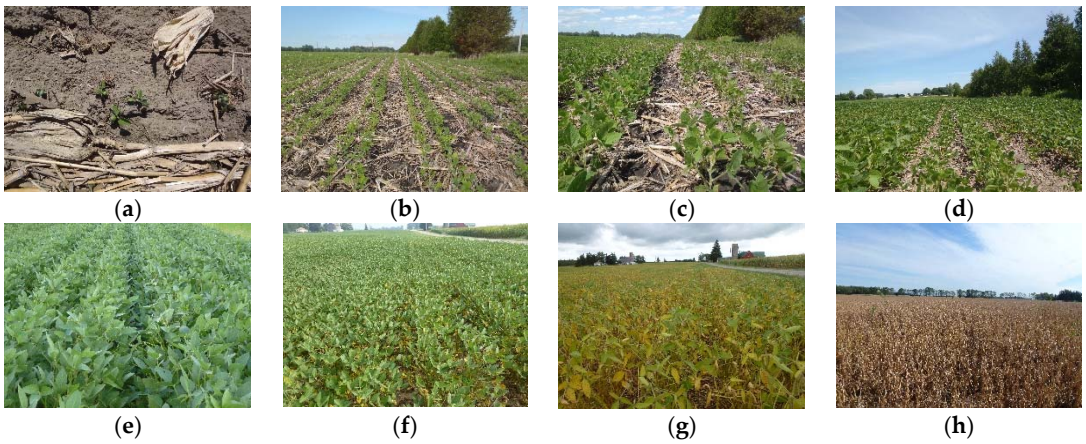

Figure 10. The ground truth photos of soybean. (**a**) May 23, (**b**) June 19, (**c**) July 2, (**d**) July 16, (**e**) August 11, (**f**) September 3, (**g**) September 13 and (**h**) September 25.

5. Discussion

5.1. Classification Performance with Only the Two Related Pairs of Decomposition Parameters

From the results in Section 4, it is clear that the ND-RF method produces better classification performance than the CP-RF method. The theoretical analysis in Section 3 shows that only two

decomposition parameters (τ, $|\delta|$) from Neumann decomposition are directly related to the two parameters (H, α) from Cloude–Pottier decomposition. For the respective third parameters, there is no direct relationship between ϕ_δ and A. Therefore, it is interesting to further check the classification performance in case only the two related pairs of decomposition parameters were used as classification features. For this purpose, the two classification methods are modified here by using two decomposition parameters instead of three decomposition parameters. The corresponding methods are named after "ND2-RF" method (τ, $|\delta|$) and "CP2-RF" method (H, α).

As shown in Table 7, the classification accuracy of ND2-RF and CP2-RF also improves with the increase of the number of images and the improvements are larger at the beginning than at the end, as it happened with ND-RF and CP-RF. However, the improvement provided by ND2-RF method over CP2-RF is very small, with the maximum case around 3%. Compared with previous classification results using all three decomposition parameters in Table 4, the classification accuracies after using the third parameter significantly increase for Neumann decomposition. However, in case of using Cloude–Pottier decomposition, the classification accuracies after adding the third parameter (A) show very similar performance, and even a little worse in some multi-temporal combinations. Therefore, τ and $|\delta|$ from Neumann decomposition provide a classification performance very close to H and α from Cloude–Pottier decomposition, which is consistent with the theoretical analysis of their physical meanings. The third parameter ϕ_δ in Neumann decomposition makes a clear impact in improving crop classification performance.

Table 7. The overall accuracy and Kappa coefficient of ND2-RF and CP2-RF classification methods with different combinations of multi-temporal RADARSAT-2 images.

Multi-Temporal Combination	Number of Images	ND2-RF		CP2-RF	
		OA (%)	Kappa	OA (%)	Kappa
20150412~20150506	2	44.38	0.31	45.15	0.32
20150412~20150520	3	57.72	0.47	57.82	0.47
20150412~20150623	4	71.47	0.63	71.42	0.63
20150412~20150703	5	75.37	0.68	73.34	0.65
20150412~20150717	6	82.21	0.77	79.11	0.73
20150412~20150810	7	83.55	0.79	81.93	0.77
20150412~20150903	8	87.39	0.84	84.64	0.80
20150412~20150913	9	90.33	0.87	89.60	0.87
20150412~20150917	10	91.18	0.89	90.91	0.88
20150412~20150927	11	91.90	0.90	91.63	0.89

5.2. Sensitivity of Training and Testing Samples on Overall Classification Performance

It is well-known that the classification performance is affected by the training and testing samples, including their distribution and numbers. To investigate the sensitivity to training and testing samples on the overall classification performance of ND-RF and CP-RF methods, the classification tests with different combinations of multi-temporal RADARSAT-2 images were carried out again by exchanging the training samples and the testing samples in Table 2. In this case, the fields and pixels for training are mostly larger than those for testing. The overall accuracy and Kappa coefficient of ND-RF and CP-RF classification methods are shown in Table 8. As in the previous tests, the classification accuracies of ND-RF and CP-RF also improve with the increase in the number of images and the improvements are larger at the beginning than at the end. The values of classification accuracies of ND-RF and CP-RF are slightly lower than the previous results in Table 4, which proves that both classification methods are sensitive to training and testing samples. However, the ND-RF method still produces better classification performance than the CP-RF method for all multi-temporal combinations in the new random scenario. It somehow reflects the robustness of the advantage of the ND-RF method over the CP-RF method for crop classification.

Table 8. The overall accuracy and Kappa coefficient of ND-RF and CP-RF with different combinations of multi-temporal RADARSAT-2 images after exchanging the training and testing samples in previous tests.

Multi-Temporal Combination	Number of Images	ND-RF		CP-RF	
		OA (%)	Kappa	OA (%)	Kappa
20150412~20150506	2	57.08	0.48	53.98	0.44
20150412~20150520	3	62.84	0.55	61.66	0.53
20150412~20150623	4	75.76	0.71	72.94	0.68
20150412~20150703	5	79.78	0.76	75.46	0.71
20150412~20150717	6	80.10	0.76	76.75	0.72
20150412~20150810	7	81.53	0.78	79.07	0.75
20150412~20150903	8	82.16	0.79	79.54	0.75
20150412~20150913	9	84.42	0.81	83.58	0.80
20150412~20150917	10	85.14	0.82	83.66	0.80
20150412~20150927	11	85.43	0.82	83.89	0.81

6. Conclusions

The Neumann decomposition is aimed at describing vegetation scattering, and two of its output parameters have physical meanings close to Cloude–Pottier decomposition outputs. To investigate the performance of Neumann decomposition on crop classification, a multi-temporal supervised classification method based on Neumann decomposition and Random Forest Classifier (named as "ND-RF") is proposed in this paper. For comparison with Cloude–Pottier decomposition, the CP-RF classification scheme is constructed by replacing the Neumann decomposition with Cloud–Pottier decomposition in ND-RF method. For experiment validation, 10 multi-temporal combinations of images from a total of 11 RADARSAT-2 images acquired over a cropland site in London, Canada in 2015 were tested by adding images one by one sequentially along the SAR observation time. As expected, the results show that the classification accuracy of ND-RF and CP-RF improve with the increase of the number of images. The largest improvements are found at the beginning, and then the changes become gradual. The ND-RF method produces better classification performance than the CP-RF method. Additional tests indicate that two parameters τ and $|\delta|$ from Neumann decomposition show very close classification performance to H and α from Cloude–Pottier decomposition, which validates the theoretical analysis about their similar physical meaning. However, the third parameter ϕ_δ in Neumann decomposition is more effective to improve the classification accuracies than the third parameter A in Cloude–Pottier decomposition. It somehow illustrates the potential advantages of Neumann decomposition on representing vegetation targets.

Author Contributions: Q.X. contributed to the design and implementation of the proposed methodology and wrote and revised the paper; J.W. and J.S. contributed to the discussion of the results and revised the paper; C.L., H.F. and X.L. discussed the results and drew some of the figures; and J.M.L.-S. contributed with some ideas and revised the paper.

Funding: This research was funded in part by the Canadian Space Agency SOAR-E program (Grant No. SOAR-E-5489), the National Natural Science Foundation of China (Grant No. 41804004, 41820104005, 41531068), the Fundamental Research Funds for the Central Universities, China University of Geosciences (Wuhan) (Grant No. CUG190633), and the Spanish Ministry of Science, Innovation and Universities, State Research Agency (AEI) and the European Regional Development Fund under project TEC2017-85244-C2-1-P.

Acknowledgments: The authors would like to thank the Canadian Space Agency and Agriculture and Agri-Food Canada for providing the RADARSAT-2 data, Josep David Ballester-Berman from University of Alicante for his helpful discussion, and Dandan Wang from Beijing Normal University for her help in ArcGIS Mapping.

Conflicts of Interest: The authors declare no conflict of interest.

References

1. Brown, L.R. *Outgrowing the Earth: The Food Security Challenge in an Age of Falling Water Tables and Rising Temperatures*; W. W. Norton & Company: New York, NY, USA, 2005.
2. McNairn, H.; Shang, J.; Jiao, X.; Champagne, C. The contribution of ALOS PALSAR multipolarization and polarimetric data to crop classification. *IEEE Trans. Geosci. Remote Sens.* **2009**, *47*, 3981–3992. [CrossRef]
3. Woodhouse, I.H. *Introduction to Microwave Remote Sensing*; CRC Press: Boca Raton, FL, USA, 2006.
4. Lee, J.S.; Pottier, E. *Polarimetric Radar Imaging: From Basics to Applications*; CRC Press: Boca Raton, FL, USA, 2009.
5. Cloude, S.R. *Polarisation: Applications in Remote Sensing*; Oxford University Press: New York, NY, USA, 2009.
6. Steele-Dunne, S.C.; McNairn, H.; Monsivais-Huertero, A.; Judge, J.; Liu, P.W.; Papathanassiou, K. Radar Remote Sensing of Agricultural Canopies: A Review. *IEEE J. Sel. Top. Appl. Earth Obs. Remote Sens.* **2017**, *10*, 2249–2273. [CrossRef]
7. Huang, X.; Wang, J.; Shang, J.; Liao, C.; Liu, J. Application of polarization signature to land cover scattering mechanism analysis and classification using multi-temporal C-band polarimetric RADARSAT-2 imagery. *Remote Sens. Environ.* **2017**, *193*, 11–28. [CrossRef]
8. Gao, H.; Wang, C.; Wang, G.; Zhu, J.; Tang, Y.; Shen, P.; Zhu, Z. A Crop Classification Method Integrating GF-3 PolSAR and Sentinel-2A Optical Data in the Dongting Lake Basin. *Sensors* **2018**, *18*, 3139. [CrossRef] [PubMed]
9. Tao, C.; Chen, S.; Li, Y.; Xiao, S. PolSAR Land Cover Classification Based on Roll-Invariant and Selected Hidden Polarimetric Features in the Rotation Domain. *Remote Sens.* **2017**, *9*, 660.
10. Sun, C.; Jiao, L.; Cheng, L.; Liu, H. Weighted Wishart distance learning for PolSAR image classification. *Int. J. Remote Sens.* **2017**, *38*, 5232–5250. [CrossRef]
11. Zhou, Y.; Wang, H.; Xu, F.; Jin, Y.Q. Polarimetric SAR Image Classification Using Deep Convolutional Neural Networks. *IEEE Geosci. Remote Sens. Lett.* **2016**, *13*, 1935–1939. [CrossRef]
12. Chen, S.; Li, Y.; Wang, X. Crop discrimination based on polarimetric correlation coefficients optimization for PolSAR data. *Int. J. Remote Sens.* **2015**, *36*, 4233–4249. [CrossRef]
13. Skriver, H. Crop classification by multitemporal C- and L-band single- and dual-polarization and fully polarimetric SAR. *IEEE Trans. Geosci. Remote Sens.* **2012**, *50*, 2138–2149. [CrossRef]
14. Skriver, H.; Mattia, F.; Satalino, G.; Balenzano, A.; Pauwels, V.R.N.; Verhoest, N.E.C.; Davidson, M. Crop Classification Using Short-Revisit Multitemporal SAR Data. *IEEE J. Sel. Top. Appl. Earth Obs. Remote Sens.* **2011**, *4*, 423–431. [CrossRef]
15. Deschamps, B.; McNairn, H.; Shang, J.; Jiao, X. Towards operational radar-only crop type classification: Comparison of a traditional decision tree with a random forest classifier. *Can. J. Remote Sens.* **2012**, *38*, 60–68. [CrossRef]
16. Sonobe, R.; Tani, H.; Wang, X.; Kobayashi, N.; Shimamura, H. Random forest classification of crop type using multi-temporal TerraSAR-X dual-polarimetric data. *Remote Sens. Lett.* **2014**, *5*, 157–164. [CrossRef]
17. Hariharan, S.; Mandal, D.; Tirodkar, S.; Kumar, V.; Bhattacharya, A.; Lopez-Sanchez, J.M. A Novel Phenology Based Feature Subset Selection Technique Using Random Forest for Multitemporal PolSAR Crop Classification. *IEEE J. Sel. Top. Appl. Earth Obs. Remote Sens.* **2018**, *11*, 4244–4258. [CrossRef]
18. Liao, C.; Wang, J.; Huang, X.; Shang, J. Contribution of Minimum Noise Fraction Transformation of Multi-temporal RADARSAT-2 Polarimetric SAR Data to Cropland Classification. *Can. J. Remote Sens.* **2018**, *44*, 215–231. [CrossRef]
19. Li, X.; Chen, Y.; Tong, L.; Luo, S. A study on vegetation cover extraction using a Wishart H-α classifier based on fully polarimetric Radarsat-2 data. *Int. J. Remote Sens.* **2016**, *1161*, 1–16. [CrossRef]
20. Jiao, X.; Kovacs, J.M.; Shang, J.; McNairn, H.; Walters, D.; Ma, B.; Geng, X. Object-oriented crop mapping and monitoring using multi-temporal polarimetric RADARSAT-2 data. *ISPRS J. Photogramm. Remote Sens.* **2014**, *96*, 38–46. [CrossRef]
21. Shimoni, M.; Borghys, D.; Heremans, R.; Perneel, C.; Acheroy, M. Fusion of PolSAR and PolInSAR data for land cover classification. *Int. J. Appl. Earth Obs. Geoinf.* **2009**, *11*, 169–180. [CrossRef]

22. Chen, S.; Li, Y.; Wang, X.; Xiao, S.; Sato, M. Modeling and interpretation of scattering mechanisms in polarimetric synthetic aperture radar: Advances and perspectives. *IEEE Signal Process. Mag.* **2014**, *31*, 79–89. [CrossRef]
23. Freeman, A.; Durden, S.L. A three-component scattering model for polarimetric SAR data. *IEEE Trans. Geosci. Remote Sens.* **1998**, *36*, 963–973. [CrossRef]
24. Yamaguchi, Y.; Moriyama, T.; Ishido, M.; Yamada, H. Four-component scattering model for polarimetric SAR image decomposition. *IEEE Trans. Geosci. Remote Sens.* **2005**, *43*, 1699–1706. [CrossRef]
25. Yamaguchi, Y.; Sato, A.; Boerner, W.-M.; Sato, R.; Yamada, H. Four-Component Scattering Power Decomposition with Rotation of Coherency Matrix. *IEEE Trans. Geosci. Remote Sens.* **2011**, *49*, 2251–2258. [CrossRef]
26. Sato, A.; Yamaguchi, Y.; Singh, G. Sang-Eun Park Four-Component Scattering Power Decomposition with Extended Volume Scattering Model. *IEEE Geosci. Remote Sens. Lett.* **2012**, *9*, 166–170. [CrossRef]
27. Singh, G.; Yamaguchi, Y.; Park, S.-E. General Four-Component Scattering Power Decomposition with Unitary Transformation of Coherency Matrix. *IEEE Trans. Geosci. Remote Sens.* **2013**, *51*, 3014–3022. [CrossRef]
28. Chen, S.; Wang, X.S.; Xiao, S.P.; Sato, M. General Polarimetric Model-Based Decomposition for Coherency Matrix. *IEEE Trans. Geosci. Remote Sens.* **2014**, *52*, 1843–1855. [CrossRef]
29. Xiang, D.; Ban, Y.; Su, Y. Model-Based Decomposition with Cross Scattering for Polarimetric SAR Urban Areas. *IEEE Geosci. Remote Sens. Lett.* **2015**.
30. Xiang, D.; Wang, W.; Tang, T.; Su, Y. Multiple-component polarimetric decomposition with new volume scattering models for PolSAR urban areas. *IET Radar Sonar Navig.* **2017**, *11*, 410–419. [CrossRef]
31. Xie, Q.; Ballester-Berman, J.D.; Lopez-Sanchez, J.M.; Zhu, J.; Wang, C. Quantitative Analysis of Polarimetric Model-Based Decomposition Methods. *Remote Sens.* **2016**, *8*, 977. [CrossRef]
32. Xie, Q.; Ballester-Berman, J.D.; Lopez-Sanchez, J.M.; Zhu, J.; Wang, C. On the Use of Generalized Volume Scattering Models for the Improvement of General Polarimetric Model-Based Decomposition. *Remote Sens.* **2017**, *9*, 117. [CrossRef]
33. Xie, Q.; Zhu, J.; Lopez-Sanchez, J.M.; Wang, C.; Fu, H. A Modified General Polarimetric Model-Based Decomposition Method with the Simplified Neumann Volume Scattering Model. *IEEE Geosci. Remote Sens. Lett.* **2018**, *15*, 1229–1233. [CrossRef]
34. Cloude, S.R.; Pottier, E. An entropy based classification scheme for land applications of polarimetric SAR. *IEEE Trans. Geosci. Remote Sens.* **1997**, *35*, 68–78. [CrossRef]
35. Lee, J.-S.; Grunes, M.R.; Ainsworth, T.L.; Du, L.J.; Schuler, D.L.; Cloude, S.R. Unsupervised classification using polarimetric decomposition and the complex Wishart classifier. *IEEE Trans. Geosci. Remote Sens.* **1999**, *37*, 2249–2258.
36. Ferro-Famil, L.; Pottier, E.; Lee, J.S. Unsupervised classification of multifrequency and fully polarimetric SAR images based on the H/A/Alpha-Wishart classifier. *IEEE Trans. Geosci. Remote Sens.* **2001**, *39*, 2332–2342. [CrossRef]
37. Neumann, M. Remote sensing of Vegetation Using Multi-Baseline Polarimetric SAR Interferometry: Theoretical Modeling and Physical Parameter Retrieval. Ph.D. Thesis, University of Rennes, Rennes, France, January 2009.
38. Neumann, M.; Ferro-Famil, L.; Jager, M.; Reigber, A.; Pottier, E. A polarimetric vegetation model to retrieve particle and orientation distribution characteristics. In *2009 IEEE International Geoscience and Remote Sensing Symposium*; IEEE: Cape Town, South Africa, 2009; pp. IV-145–IV-148.
39. Neumann, M.; Ferro-Famil, L.; Reigber, A. Estimation of Forest Structure, Ground, and Canopy Layer Characteristics from Multibaseline Polarimetric Interferometric SAR Data. *IEEE Trans. Geosci. Remote Sens.* **2010**, *48*, 1086–1104. [CrossRef]
40. Neumann, M.; Saatchi, S.S.; Ulander, L.M.H.; Fransson, J.E.S. Assessing Performance of L- and P-Band Polarimetric Interferometric SAR Data in Estimating Boreal Forest Above-Ground Biomass. *IEEE Trans. Geosci. Remote Sens.* **2012**, *50*, 714–726. [CrossRef]
41. Lee, J.-S.; Ainsworth, T.L. The Effect of Orientation Angle Compensation on Coherency Matrix and Polarimetric Target Decompositions. *IEEE Trans. Geosci. Remote Sens.* **2011**, *49*, 53–64. [CrossRef]

42. Breiman, L. Random Forest. *Mach. Learn.* **2001**, *45*, 5–32. [CrossRef]
43. Pal, M. Random forest classifier for remote sensing classification. *Int. J. Remote Sens.* **2005**, *26*, 217–222. [CrossRef]